Piezotronic Activity Study by AFM Tip (Al) Top Electrode of Single ZnO Nanofiber Deposited on TiN_x/c-Si Substrate

F. Bechiri[a,b], Y. Bakha[c,*] and M. Zerdali[b]

[a] *Université Abd el Hamid Ibn Badis de Mostaganem, Département de Génie Electrique, Faculté des Sciences et de la Technologie, Route de Belhacel, BP 27000, Mostaganem, Algeria*
[b] *Université des Sciences et de la Technologie d'Oran Mohamed Boudiaf, Departement Technologie des Matériaux, Laboratoire de Microscopie Electronique & Sciences des Matériaux, Faculté de Physique, BP 1505 El Mnaouer, USTO MB, BP 31123, Oran, Algeria*
[c] *Plateforme Technologique en Microsystémes Electromecaniques (P-MEMS), Centre de Développement des Technologies Avancées (CDTA), Cité du 20 août 1956 Baba Hassen, BP 16081, Alger, Algeria*

Received: 25.03.2024 & Accepted: 24.06.2024

Doi: 10.12693/APhysPolA.146.174 *e-mail: ybakha@cdta.dz

ZnO nanofibers were synthesized via a hydrothermal method. A single nanofiber was delicately transferred and deposited onto a TiN_x thin film on a silicon substrate to facilitate the investigation of its piezotronic properties. An aluminum-coated atomic force microscope tip was employed in contact mode as a top nanoscale electrode to locally induce bending deformation in the individual ZnO nanofiber. The current–voltage (I–V) characteristics recorded between the top atomic force microscope tip electrode and the bottom TiN_x surface exhibited rectifying behavior, indicative of the formation of a Schottky junction upon the application of a minimum bending force of 25 nN by the atomic force microscope tip. This force threshold was necessary to ensure adequate contact between the atomic force microscope probe and the ZnO nanofiber. However, upon exceeding the 25 nN bending force perpendicular to the c-axis, the forward current underwent a substantial reduction, eventually leading to complete suppression of the Schottky junction under further increments in the bending force. Finite element method simulations elucidated the presence of piezoelectric activity within the ZnO nanofiber, which was responsible for the observed attenuation in the forward current. The Cheung–Cheung method was employed to quantify the increase in barrier height at the Schottky junction as a function of the applied bending force.

topics: ZnO nanofibers (ZnO-NFs), atomic force microscope (AFM), I–V, piezopotential

1. Introduction

Zinc oxide (ZnO) has emerged as a ubiquitous material in numerous research endeavors involving ZnO nanostructures (ZnO-NSs). Conventionally, ZnO-NSs can be synthesized via various techniques, including catalyst-assisted methods and the vapor–liquid–solid (VLS) process [1].

However, the hydrothermal approach has gained significant traction due to its inherent advantages, such as low-temperature growth conditions, simplicity, and cost-effectiveness [2]. Furthermore, this method offers a facile route to fabricate ZnO nanostructures with diverse morphologies at low temperatures [3], enabling the exploitation of their unique properties for various applications, including optoelectronic [4] and piezoelectric devices [5]. Consequently, a facile hydrothermal synthesis protocol is proposed for the fabrication of ZnO nanofibers (ZnO-NFs), which are subsequently integrated into a Schottky diode structure comprising an aluminum-coated atomic force microscope (AFM) tip as the top electrode, the ZnO-NF as the active channel, and a TiN_x thin film as the bottom electrode, which is compatible with Si integrated circuit. Schottky diode based on such configuration (AFM tip (Al)/ZnO-NF/TiN_x) has garnered significant research interest due to its potential for investigating the electron transport properties along the c-axis [6].

The theoretical study conducted on the c-plane surface of ZnO nanostructure elucidates that the Schottky barrier heights (SBHs) at the metal/ZnO interface exhibit a pronounced sensitivity to the specific chemical bonding configurations present at the interface [7]. Such surface is chemically reactive, and the formation of interfacial metal–zinc bonds ($+c$, Zn^+-terminated top surface) tends to facilitate Ohmic contact behavior, while the contribution of metal–oxygen bonds ($-c$, O^--terminated top surface) is contingent upon the nature of the specific metal. Many reports have affirmed that the c-plane ZnO nanostructure surface engaging in metal–oxygen or metal–zinc bonds tends to promote Ohmic contact characteristics with Al or titanium (Ti) metals [8]. Whereas noble or inert metals such as Ag, Pt, Au, and Pd exhibit Schottky-like rectifying behavior [9], ZnO-NF on the contrary offers lateral surface, i.e., m-plane and a-plane, which are non-polar surfaces and exhibit less chemical reactivity than c-plane, as reported by Jae Wook Lee et al. [10].

Additionally, non-polar ZnO surfaces are known to have a high density of structural defects [11]. The current–voltage (I–V) analysis of surface states of ZnO nanowires (ZnO-NWs) confirmed that the Fermi level is pinned, which is primarily caused by surface states, leading to an SBH of 0.34–0.37 eV [12].

This research aims to explore and realize piezosensor based on AFM tip (Al) and lateral surface of ZnO-NF initially constructed to establish a Schottky contact at one end and an Ohmic contact at the other end by selecting metals such as TiN_x with appropriate work functions. As depicted above, the laterals surface of ZnO-NF is featured by inert planes and defect states. The presence of ZnO-NF makes the interface less reactive toward the Al electrode, and the situation corresponds closely to the Schottky-like rectifying behavior interface [13].

The Schottky contact between the metal contact and ZnO-NF is a crucial component of current modulation [14]. Therefore, the modulation of SBH through Schottky contacts is one of the key factors in the context of piezoelectric sensors. We expect that such a configuration is more favorable to obtain Schottky-like rectifying behavior, accompanied by more significant SBH and comparable to noble metal [15].

As a result, ZnO-NFs are seen as promising components for energy harvesting applications, showing potential for use in piezoelectric sensor devices and the development of highly sensitive cutting-edge sensors.

2. Experimental setup

ZnO nanostructures were synthesized via a hydrothermal process, employing a Zn^{2+}/OH^- ratio of 1/20. The proposed protocol offers a simplified approach compared to alternative methods that often involve the use of complex and potentially hazardous chemical precursors [16]. The synthesis procedure involved the preparation of two distinct solutions, denoted as A and B. Solution A was obtained by weighing out zinc chloride ($ZnCl_2$) and subsequently dissolving it in 10 mL of deionized (DI) water. This solution was subjected to continuous stirring at 40°C for 15 min to ensure the formation of a clear and homogeneous mixture. Concurrently, a sodium hydroxide (NaOH) solution was prepared and maintained under stirring conditions to facilitate complete dissolution in a polytetrafluoroethylene (PTFE) beaker at a temperature of 40°C. Solution B was formulated by dissolving polyethylene glycol (PEG) in 105 mL of DI water. Additionally, solution A was subjected to continuous stirring at 40°C for 15 min to ensure the formation of a clear and homogeneous mixture. Subsequently, solution A was carefully introduced dropwise into solution B under constant stirring. The resulting mixture yielded a clear and transparent solution, potentially attributable to the formation of $Zn(OH)_4^{-2}$ precursor complexes, which serve as the building blocks for the growth of ZnO-NFs. The final solution was transferred into a sealed tubular container and placed in an oven maintained at 90°C for a duration of 3 h to facilitate the growth of ZnO nanofibers (ZnO-NFs). The temperature regulation during the hydrothermal synthesis was precisely controlled within ± 1°C. Subsequent to the growth process, the resulting white precipitate was separated from the solution by centrifugation at 7000–9000 rpm and then rinsed with deionized (DI) water to remove residual salt byproducts. This washing cycle was repeated multiple times until a solution with a neutral pH was obtained. The collected white precipitate was then air-dried at 45°C for 1 h. The resulting white powder was carefully harvested for further characterization analyses.

The morphological features of the as-synthesized material were investigated using scanning electron microscopy (SEM, JEOL — JSM-6610LA). Furthermore, the crystallographic structure of the powder was analyzed by X-ray diffraction (XRD) employing a θ–2θ configuration on an Empyrean PANalytical diffractometer equipped with a Cu $K_{\alpha,1}$ radiation source ($\lambda = 0.154058$ nm).

For the characterization processes, the as-synthesized ZnO nanostructured powder was dispersed in ethanol, and a droplet of the suspension was extracted and deposited onto a silicon surface. Upon complete evaporation of the ethanol solvent, the nanostructures were uniformly distributed on the surface, facilitating subsequent analyses. Specifically, for scanning electron microscopy (SEM) characterization, the ZnO-NFs were gently transferred onto an n-type silicon substrate. However, for X-ray diffraction (XRD) pattern acquisition, the ZnO-NWs were deposited on glass substrates. To record the current–voltage (I–V) characteristics, the ZnO-NWs were delicately deposited onto a conductive TiN_x thin film.

The atomic force microscopy (AFM, JEOL) equipment was employed in contact mode to facilitate the observation and recording of I–V characteristics of the ZnO-NFs. The device structure comprised an aluminum-coated AFM tip as the top electrode, the ZnO-NF as the active channel, a TiN_x thin film as the bottom electrode, and a crystalline

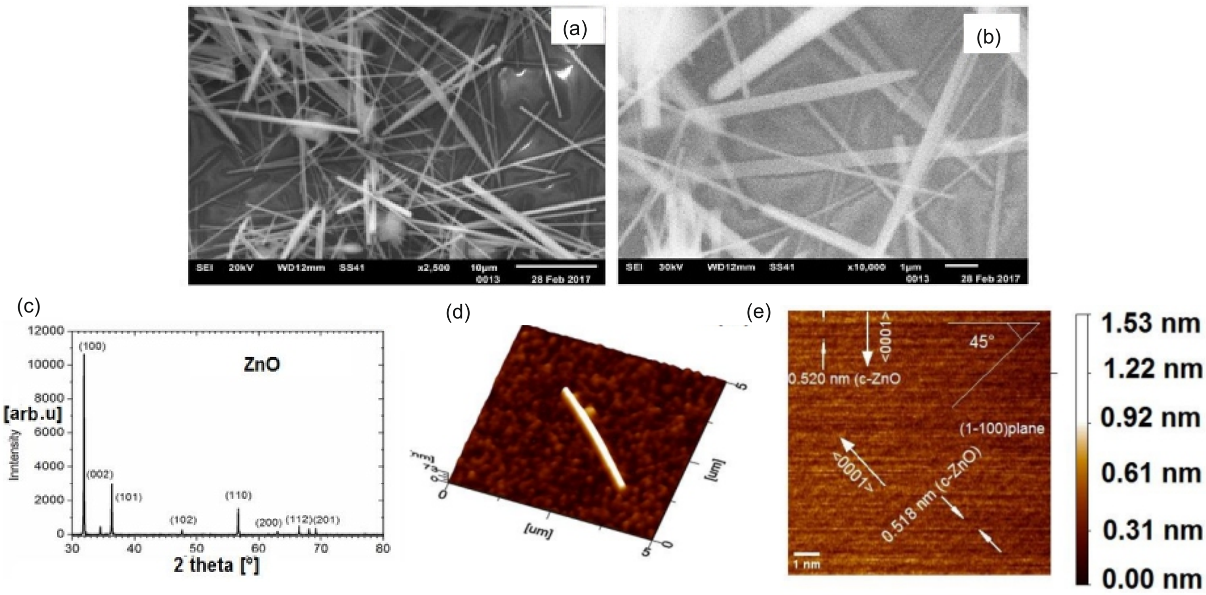

Fig. 1. SEM images of ZnO-NFs grown at 90°C (a) at a magnification of 2500; (b) enlarged observation of ZnO-NF at a magnification of 10000. (c) XRD patterns of ZnO-NFs prepared by hydrothermal method with an atomic concentration ratio of 1/20. (d) AFM tapping mode of 5×5 μm^2 scan area. Single ZnO-NF deposited on c-Si substrate. (e) High-resolution imaging carried out in AFM contact mode of the lateral surface plane (1−100) of ZnO-NF, indicating two stacked blocks tilted by 45°. The lattice parameter c indicates along crystallographic direction ⟨0001⟩.

silicon (c-Si) substrate. The TiN_x thin films were deposited onto (100)-oriented silicon substrates via DC sputtering using an MRC 643 system. Measurements of I–V were performed at room temperature in the dark to neglect the effect of the photoconductivity.

3. Result and discussion

3.1. Structural characterization

Figure 1a and b shows SEM images of ZnO-NFs prepared with 1/20 molar ratio at two different magnifications. The structure is formed by separated and elongated ZnO-NFs. The growth of ZnO-NFs is straight up, and the aspect ratio (length to width) of ZnO-NFs is extended to the value of 50. The proposed molar ratio of 1/20 enables the growth of ZnO-NFs units and makes it easy to drive elongated ZnO-NFs parallel to [002] direction. Figure 1c shows XRD patterns of ZnO-NSs synthesized at an atomic ratio of 1/20. Diffraction peaks are identified thanks to the JCPDS card number no. 89-0510 [17], highlighting the ZnO wurtzite phase. We observe a strong enhancement of (100) peak intensity and narrow full-width at half-maximum (FWHM).

Moreover, the presence of (100) peak implies elongated ZnO-NFs. This result is correlated with AFM images (Fig. 1d), where a single ZnO-NF is observed in a downward position through a scan area of 5×5 μm^2. High-resolution imaging of the lateral surface plane (1-100) of the lateral surface of ZnO nanofiber (ZnO-NF) is presented in Fig. 1e, encompassing a scanned area of 10×10 nm^2. The surface exhibits a remarkably flat morphology, characterized by an average roughness of 0.31 nm. The in-plane is characterized by a translational period of ZnO along the two blocks. The stacking sequence planes are parallel to crystallographic direction ⟨0001⟩ with an average spacing of 0.520 nm (marked by white arrows), which is very close to the c-ZnO lattice parameter. Furthermore, the growth of the ZnO-NF proceeds along the c-axis (⟨0001⟩ direction), manifesting as a structure composed of two stacked blocks oriented at a 45° tilt with respect to each other. Notably, each block is aligned parallel to the crystallographic ⟨0001⟩ direction. This distinctive geometric configuration gives rise to the presence of structural defect states within the nanofiber known as stacking faults (SFs), which are common in non-polar ZnO-plane grown along ⟨0001⟩ direction.

3.2. Electrical characterization

Figure 2a shows the experimental setup used to record the I–V characteristics of a single ZnO-NF. In order to ensure a closed loop of the circuit, TiN_x film is connected to the ground. The stiffness of the

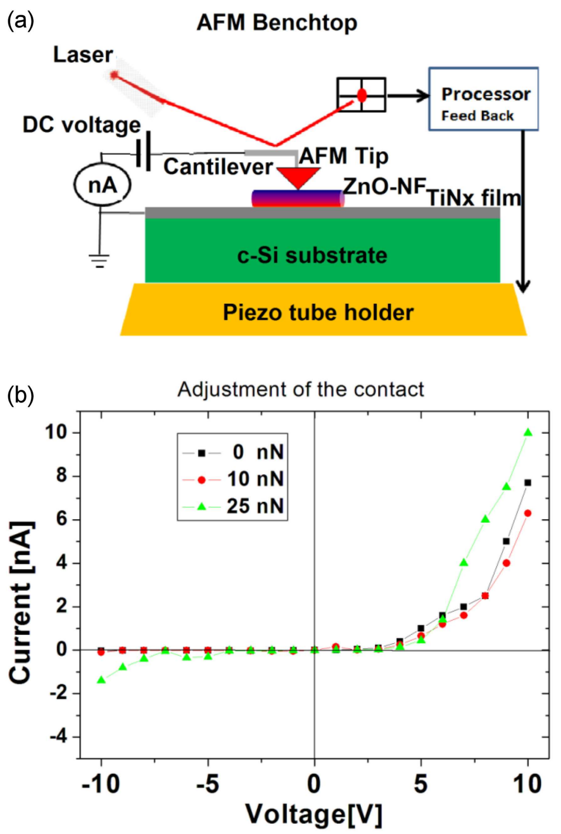

Fig. 2. (a) Schematic diagram of experimental setup. (b) I–V characteristics and contact adjustment of the device, including AFM tip (Al) /ZnO-NW/TiN_x thin film up on Si substrate.

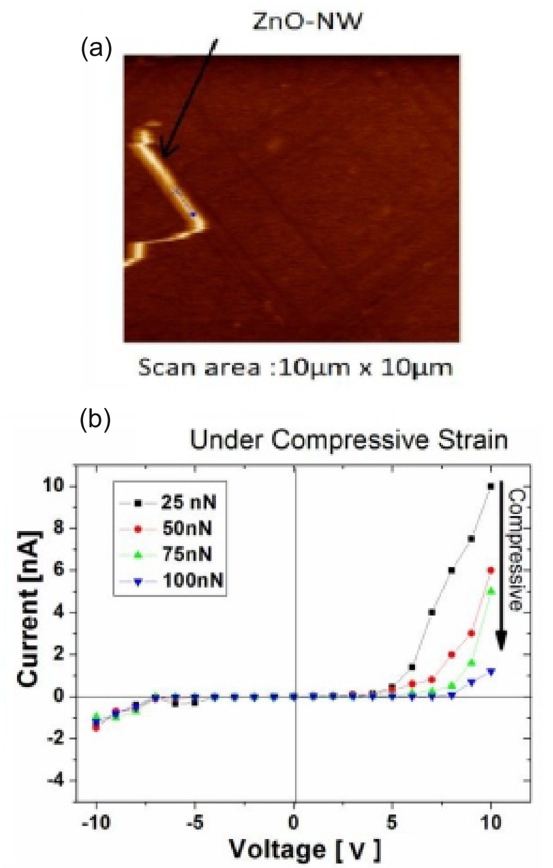

Fig. 3. AFM topography and I–V characteristics under AFM configuration: (a) AFM scan of ZnO-NW in contact mode, (b) effect of different transverse forces applied by the AFM tip upon ZnO-NW on I–V characteristics.

cantilever is 5 N/m in order to firmly hold the AFM tip on top of ZnO-NF (contact mode). Afterward, the AFM tip is approached gently upon the ZnO-NF surface.

Figure 2b shows I–V characteristics of the structure, including AFM tip (Al)/ZnO-NF/TiN_x/ Si substrate. The rectification behavior of a typical Schottky at forward voltages is clearly distinguishable. The junction exhibits a threshold voltage at 8 V, which seems to be mainly due to the surface defect states wrapping the ZnO-NF surface. Indeed, the side junction formed by TiN_x/ZnO exhibits Ohmic contact, with the electron affinity of ZnO (4.35 eV) [18] being much closer to the work function of TiN_x (4.40 eV) [19]. Otherwise, the Schottky contact is formed at the edge of the AFM tip (Al) and ZnO-NF due to the pinning contact caused by surface states [20] and the non-polar nature of the lateral surface of ZnO-NF [21]. The depletion area is obviously extended on the ZnO-NF side. In summary, a minimum transverse force of 10 nN is required to guarantee a hard contact.

Figure 3a shows isolated ZnO-NW observed by AFM with a scan area of 10×10 μm^2. Such ZnO-NF will be used to record I–V characteristics under different forces.

Figure 3b shows experimental I–V characteristics, where rectifying contact behavior is observed in the forward direction. The bottom contact of the ZnO-NF remains fixed, while the top surface is left unconstrained. The I–V characteristics are measured under both strained and unstrained conditions. We have observed that excessive bending results in a significant reduction in current intensity, eventually leading to the complete blocking of forward current. Such junction is well described in the reverse and forward regions by the following equation [22]

$$I = I_s \left[\exp\left(\frac{qV - R_s I}{n k_{\mathrm{B}} T} \right) - 1 \right], \qquad (1)$$

where $I_s = AA^* T^2 \exp(q\phi_B/(k_{\mathrm{B}}T))$, and n, k_{B}, q, V, A^*, T, and ϕ_B are ideality factor, Boltzmann's constant, elementary charge, applied voltage, Richardson's constant, temperature, and barrier height, respectively. The term $R_s I$ in (1) is the voltage drop across series resistance R_s of the structure, and A is the surface area of the junction.

As shown in Fig. 3b, the forward current decreases when further compressive strain is applied.

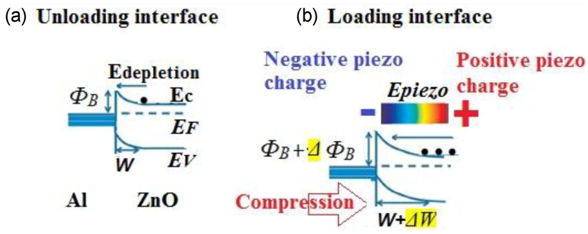

Fig. 4. Band structure of the sensor AFM tip (Al)/ZnO-NF under (a) unloading and (b) loading compression strain conditions. Black dots indicate free electrons driven on the opposite side of E_{piezo} generated by compression strain.

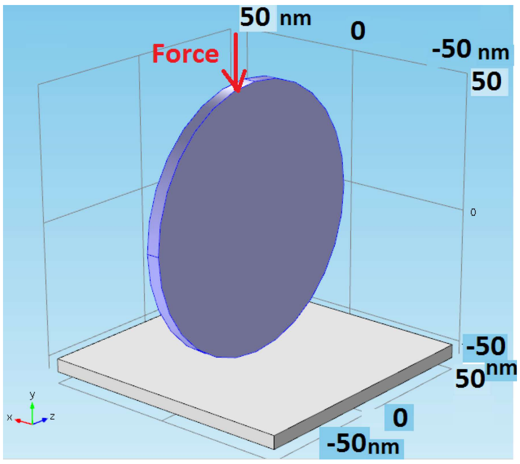

Fig. 5. Schematic model of a section of ZnO-NW carried out by FEM method, 3D side view of the excited top part of ZnO NW.

Our research on this behavior is directed towards the coupling of piezoelectric and semiconducting properties. The decrease in the forward current intensity occurs due to the increase in the barrier height ϕ_B [eV] when a different transversal force is applied by the AFM tip.

While force is absent, the junction is featured by the presence of only an electrical barrier ϕ_{B_0} due to the Schottky contact. The force induces compressive strain that probably generates a supplement barrier height $\Delta\phi_B$.

Figure 4 shows the Schottky barrier diagram where piezoelectric properties are able to increase the barrier height (Fig. 4b) through the piezoelectric field E_{piez} (drawn as a colored bar) at the side of AFM tip (Al)/ZnO-NF. Obviously, compression strain conditions (empty red arrow in Fig. 4b) should be present to fullfill such behavior. The depletion field, depicted in Fig. 4a, induces an increase in the effective barrier height, repelling electrons from the metal/ZnO-NF interface. This effect is amplified under forward bias, further diminishing the current flow. The combined influence of the enhanced depletion field and heightened barrier obstructs charge carrier transport across the junction, substantially reducing the forward current density.

In order to emphasize the presence of such a "piezo" field, we used the finite element method (FEM) carried out by COMSOL Multiphysics software (ver. 5.5). For this purpose, the piezoelectric and elastic properties of ZnO-NW are considered in the model. The calculations solve the constitutive equations that relate the stresses T_{ij} to the strains S_{kl} in anisotropic media through the following equations

$$T_{ij} = C_{ijkl}S_{kl} - e_{ijk}S_{jk}, \quad (2)$$

$$D_i = \varepsilon_{ij}E_j + e_{ijk}S_{jk}, \quad (3)$$

where D_i is the electric displacement, and E_j is the electric field. The coefficients C_{ijkl} are the components of the stiffness tensor, and the coefficients e_{ijk} are the electromechanical coupling tensor. The stiffness and piezoelectric tensor elements are reduced to a few elements due to hexagonal symmetry [23]. The constants ε_{ij} are the effective permittivity tensor.

However, there is an important detail that should be considered to carry out the FEM-COMSOL simulation. Obviously, the contact area between the AFM tip and ZnO-NF is more realistic when the touching area is limited to the size of the AFM tip. If the AFM tip touches the nanowire, the contact area is very small, so the force is applied to the shell element of the small cylinder.

ZnO-NFs shown in SEM (Fig. 1a) are featured by smooth facets. Therefore, considering ZnO-NW as a cylinder seems a good approximation. The same assumption was made in the previous work, where the ZnO-NF was considered in terms of cylinder geometry [24].

Figure 5 shows the schematic configuration where a cylinder of 50 nm radius is considered to simulate the bending and piezo characteristics in the localized area just below an AFM tip. The force is applied at the center of ZnO-NF, and the stressed size is equivalent to the curvature radius of the AFM tip (8 nm). The top part of ZnO-NF is considered free, and the bottom part is fixed to TiN_x film. The magnitudes of the applied forces are 25, 50, 75, and 100 nN. Finally, we assume the surface element at the bottom (TiN_x film) with no free electrical charges as an electrical boundary condition. The electrical connection between the bottom electrode (TiN_x) and the ground potential is established, facilitating the flow of charges and ensuring a stable reference point.

Figure 6 shows the simulation results, taking into account the boundary conditions. It is clearly seen that the range of the applied force is able to generate displacements and piezopotential along the ZnO-NF diameter. Consequently, further force increases the magnitude of the displacement; a maximum value reaches 0.86 nm, recorded at the surface for 100 nN force. The displacement magnitude

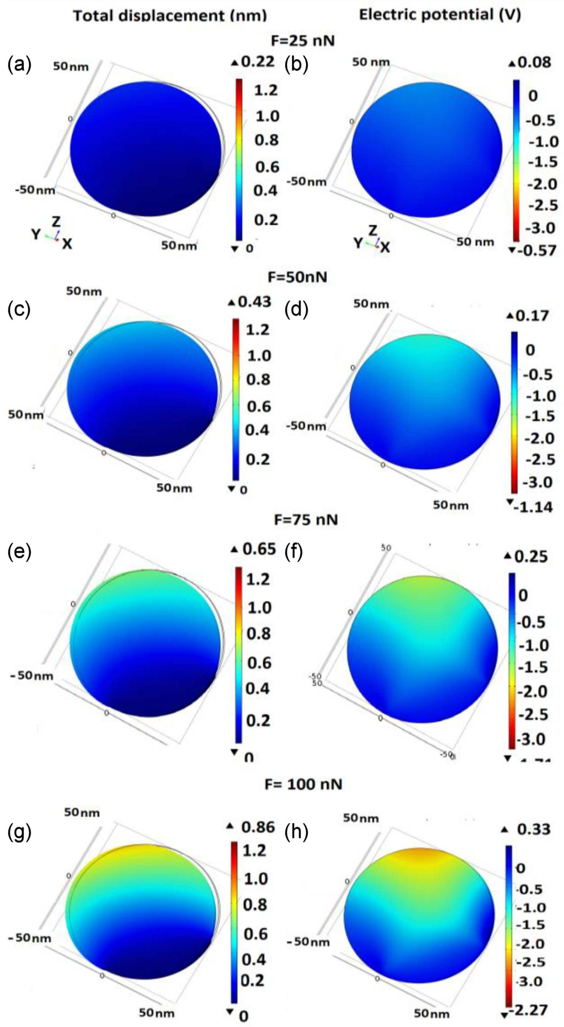

Fig. 6. FEM-COMSOL simulation applied to ZnO-NF bent by different forces along the radius. (a, c, e, g) Total displacement profile along the section of ZnO-NW. (b, d, f, h) Electrical potential distribution along the section of ZnO-NW.

is related to the induction of an electrical potential due to the piezoelectric effect. The maximum value of piezopotential is -2500 mV near the edge of an AFM tip when the applied force is 100 nN.

According to the results of our simulation (see Fig. 6c), the surface of ZnO-NF is strained by a sufficient external force, and piezoelectric property is activated (force $>$ 25 nN). Therefore, negative and positive piezopotentials are immediately created on the top AFM tip electrode and the bottom TiN_x electrode, respectively. Hence, it is possible to induce the E_{piez} field between the top of ZnO-NW (negative piezocharges) and the bottom (positive piezocharges), and such a situation is well described in Fig. 4b. Consequently, a compressive transverse strain exerted by a sharp tip on a nanowire (NW) introduces local modifications (elongation) of interatomic distances along the polar c-axis, perpendicular to the direction of stress.

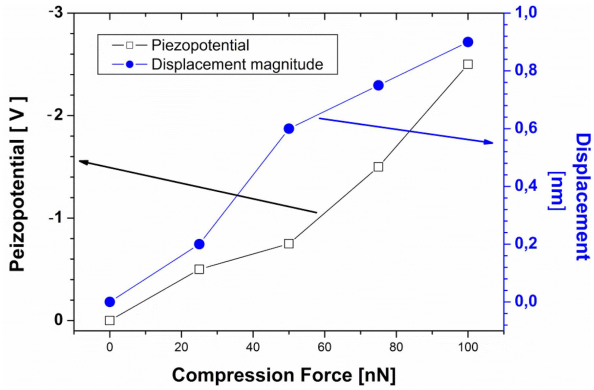

Fig. 7. FEM simulation of piezopotential output and displacement as a function of the total applied force exerted by the AFM tip (Al) upon ZnO-NF.

Figure 7 illustrates the summary of our FEM simulation plotting piezopotential as a function of the displacement magnitude of the ZnO-NF under different applied forces. The displacements are outlined in Fig. 6a, c, e, g. As expected, both the displacement and the output potential increase linearly with the applied force. By analyzing Fig. 7, we can observe that a maximum force of 100 nN is equivalent to a maximum piezopotential of -2500 mV.

Such a result is consistent with a previous work reported by Tao et al. [25], where they found from simulation results that the piezopotential of ZnO-NW linearly increases as the force increases. Additionally, R. Hinchet et al. [26] simulated ZnO-NW with a radius of 34 nm, and they found a piezopotential close to 2000 mV under an applied force of 80 nN, which is somewhat close to our result. According to Fig. 7, the sensitivity could be calculated as well using $S = \frac{\Delta V}{\Delta F}$. In our work, the estimated value of S is 26.7 mV/nN, which is twice as large as that calculated by R. Hinchet et al. [26] (11 mV/nN). Such difference might be probably due to the high aspect ratio difference. Our geometry assumed ZnO-NFs with a length of about 5 μm and a radius of 50 nm. Whereas in the simulations in [26], a length of 600 nm and a radius of 24 nm were proposed.

Additionally, Lin Zhu et al. [27] observed the aspect ratio impact on such piezopotential parameter simulated on nanorod. For the geometry of a nanorod they adopted, where the side length is less than 200 nm, the piezopotential increases rapidly with the decrease in side length under a constant force of 200 nN. The calculated piezopotential was about 2500 mV for nanorods of 60–70 nm side length. The simulation results they obtained also indicated that nanorods with a large aspect ratio have stronger radial stress, leading to a larger piezopotential. Consequently, a high aspect ratio offers a larger piezopotential response, such as reported by previous work [28, 29].

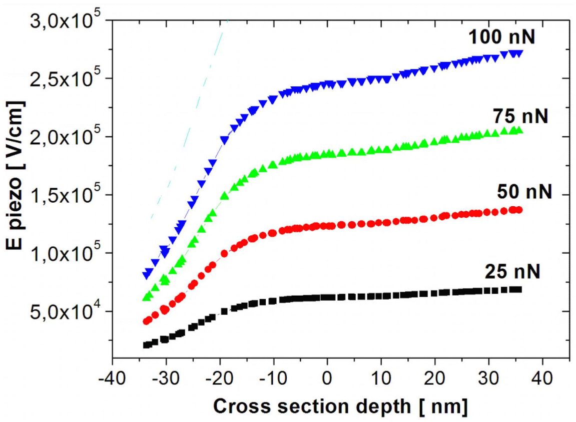

Fig. 8. Calculation of piezoelectric field along the cross-section of ZnO-NW for the set of applied forces. The diameter of ZnO-NW is 100 nm.

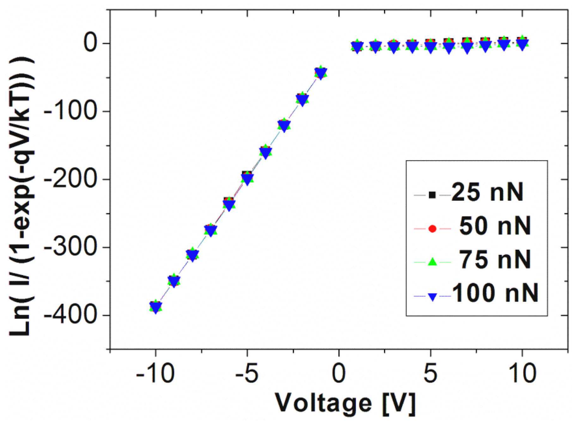

Fig. 9. Linear plots of $I/[1-\exp(-qV/(k_{\mathrm{B}}T))]$ characteristic as a function of bias voltage at room temperature for different applied forces.

Although the barrier height ϕ_B is well described by the equation relating ϕ_B at the Schottky contact and tensile or compressive straining [30], one can qualitatively emphasize ϕ_B [eV] expressed as follows

$$\phi_B = \phi_{B0} - \frac{q\, e_{15}\, \varepsilon_\perp W_{\mathrm{piez}}}{2\varepsilon_s}. \tag{4}$$

The term ϕ_{B0} expresses the barrier height dependent on the depletion layer when the strain is absent. However, the second term expresses the piezoelectric contribution of the piezocharges distributed of width W_{piez}. The strain $\varepsilon_\perp$ originates from compressive force transverse to the c-axis and is induced by the AFM tip. The constant e_{15} is the piezoelectric coefficient from the tensor element [31], and ε_s and q are the permittivity and the elementary charge, respectively.

Thus, the barrier height difference is expressed as follows

$$\Delta\phi_B = \phi_B - \phi_{B0} = -\frac{qW_{\mathrm{piez}}}{(2\varepsilon_s/e_{15})}\, \varepsilon_\perp(\%). \tag{5}$$

It is easy to see that the negative sign of strain $\varepsilon_\perp$ (compression) increases the value of ϕ_B, while the positive strain (tensile) decreases the magnitude of ϕ_B. Such electrical characteristics were observed by Qiuhong Yu et al. [32]. In Ag/ZnO nanowire and Ag/HfO_2/ZnO junctions, they observed that the current increased instead of decreasing when the tensile strain conditions were present. Such a case is possible due to barrier height reduction under the tensile strain conditions, as noted by (5). Consequently, compressive strain exerted by the AFM tip rises $\Delta\phi_B$ as demonstrated by the FEM simulation. Subsequently, barrier height makes the space charge (SC) widen and is extended deeper in ZnO-NW when compressive strain is present (see Figs. 4 and 6).

As is clear from the study carried out by the FEM simulation, the field E_{piez} can be identified by the following expression [33]

$$E_{\mathrm{piez}} = \frac{e_{15}\varepsilon_\perp}{\varepsilon_s}. \tag{6}$$

The sign of strain $\varepsilon_\perp$ tunes the magnitude and changes the direction of E_{piez}, respectively.

However, a compressive transverse strain exerted by a sharp tip on an NW introduces local modifications (elongation) of interatomic distances along the polar c-axis, perpendicular to the direction of stress, and this is the source of the generation of piezoelectric field.

Figure 8 shows clearly the magnitude of such E_{piez} along the section of ZnO-NW. Based on the FEM simulation, we have calculated the distribution of E_{piez} along the section of ZnO-NF for different applied forces. The set of E_{piez} is constant along ZnO-NF and vanishes near the grounded electrode (TiN_x electrode).

The piezoelectric study of ZnO-NF by FEM highlights the presence of E_{piez} along the cross-section of the ZnO-NF, which increases when the AFM tip force increase. As showcased from FEM results (see Fig. 6d), the direction of E_{piez} is favorable to enhance the reverse direction, therefore, it is expected that the current decreases along the section of ZnO-NF. Thus, E_{piez} is superimposed to the electric field of the junction AFM tip/ZnO-NW and increases barrier height ϕ_B (see Fig. 4b).

A force below 25 nN at the junction is slightly considered an unloaded interface. As reported by Liu et al. [34], as compressive force is incrementally augmented, this intrinsic potential barrier ϕ_B becomes progressively elevated. The presence of such a piezo field raises the barrier height ϕ_B between the AFM tip and ZnO-NF, thereby attenuating the magnitude of the net external electric field responsible for driving the current from the AFM tip (Al) toward the TiN_x electrode.

Moreover, to estimate experimentally the value of barrier height, we have used for the first time the Cheung–Cheung method [35] to extract the junction parameters of the AFM tip (Al)/ZnO-NW/TiN$_x$ structure. Such a method is powerful and very popular in investigating the electrical properties of different junctions and hetero-structures featured by series resistance R_s [36]. The method is based on the determination of the following parameters: the ideality factor n, series resistance R_s, and threshold voltage ϕ_B in the forward region ($V > 8$ V).

Figure 9 shows plots of the set of I–V curves. The presence of two distinct regions is clearly visible. In the reverse region, an interval voltage from $V = -10$ V to $V = 0$ V is a straight line, covering a wider range of the curve from which the ideality factor n can be determined.

The value of n in the reverse region is determined from the dependence $\ln(I/[1 - \exp(-qV/(k_\mathrm{B}T))])$ versus V and takes the slope of the linear region. The ideality factor n is expressed as follows

$$n = \frac{q}{k_\mathrm{B}T}\frac{\mathrm{d}V}{\mathrm{d}\ln(I)}. \tag{7}$$

The value of n is equal to 1.02 and is independent of the applied transverse force. The magnitude of n confirms thermionic diffusion mechanisms in the reverse region.

However, in the forward region, the junction exhibits a rectification behavior for bias voltage $V > 0$ V. The curves deviate considerably from linearity due to different phenomena, such as R_s.

The ideality factor n and R_s contribute to the following expression

$$\frac{\mathrm{d}V}{\mathrm{d}\ln(I)} = n\frac{k_\mathrm{B}T}{q} + R_s I. \tag{8}$$

Equation (8) allows for linear extrapolation when compared to the experimental I–V measurements obtained through I–V testing (see Fig. 10(a)). By plotting (8) as a function of I [nA], R_s is obtained as the slope of (8), and the value of the ideality factor n is extracted from the quantity $n\frac{k_\mathrm{B}T}{q}$, which represents the intercept of the linear extrapolation with the y-axis at $I = 0$ [nA]. However, in order to estimate ϕ_B, the function $H(I)$ is defined as follows

$$H(I) = V - n\frac{k_\mathrm{B}T}{q}\ln\left(\frac{I}{AA^*T^2}\right). \tag{9}$$

The function $H(I)$ is plotted versus I and gives also a straight line, while the intercept of the y-axis is equal to $n\phi_B$. For a given parameter n, ϕ_B is totally determined by

$$H(I) = n\,\phi_B + R_s I. \tag{10}$$

We assume A^* as the effective Richardson's constant of 32 A/(cm^2 K^2) [37] (A is the contact area) and $T = 273$ K.

Figure 10a shows the plots of $\frac{\mathrm{d}V}{\mathrm{d}\ln(I)}$ as a function of the current I for a set of applied forces: 25, 50, 75, and 100 nN. Hence, the ideality factor for the Schottky junction in the forward direction at 25, 50, 75, and 100 nN are 9.7, 12.4, 15.1, and 17.5, respectively. The high value of n is due to the high series resistances $R_s \times 10^7$) [Ω] that block the junction when excess compressive strain is applied.

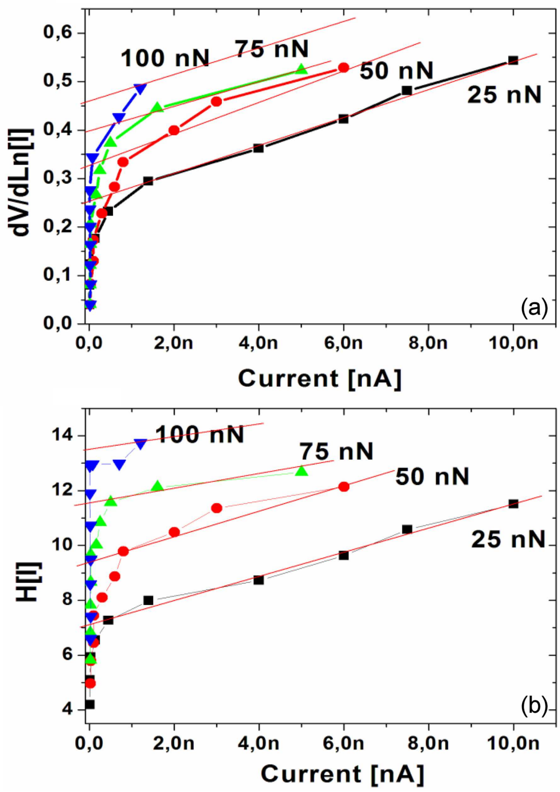

Fig. 10. (a) Experimental and simulated $\frac{\mathrm{d}V}{\mathrm{d}\ln(I)}$ versus I of AFM tip/ZnO-NW/TiN$_x$ junction under different forces in order to evaluate n. (b) Experimental and simulated $H(I)$–I plot of AFM tip/ZnO-NW/TiN$_x$ junction under different forces in order to evaluate the barrier height.

Figure 10b shows the plot of $H(I)$ versus I in order to evaluate the value of the y-axis intercept equal to $n\,\phi_B$.

According to the slope $\frac{\mathrm{d}V}{\mathrm{d}\ln(I)}$ determination, $H(I)$ function, the Schottky barrier height (SBH) of AFM tip/ZnO-NF junction is of about 0.726, 0.753, 0.762, and 0.776 eV corresponding to 25, 50, 75, and 100 nN, respectively.

Our barrier height values are in complete accordance with data found by Peter Keil et al. [38] for low compression strain while studying ZnO single crystal. I–V characteristics measurements were carried out on Metal/ZnO crystal using both O- and Zn-terminated top surfaces.

In [38], the Ag silver top electrode is deposited by sputter deposition on both surfaces of the crystal. Following the thermionic analysis, the barrier height of the metal-semiconductor contact was found to be 0.720 eV on the O-terminated top surface. Also, Keil et al. [38] observed a small decrease in the conductivity under 5 MPa compressive strain. They concluded that such barrier height

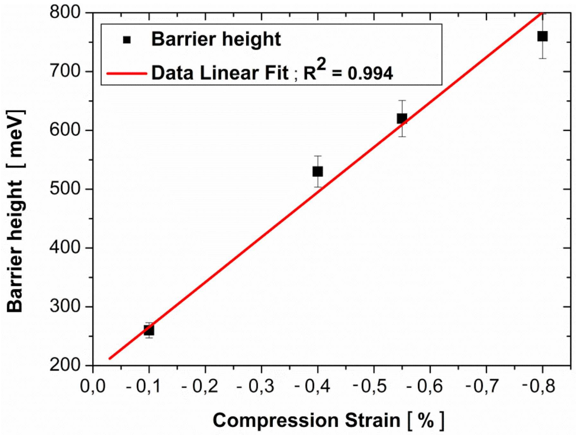

Fig. 11. Plot of the Schottky barrier height as a function of the compression strain determined by the FEM-COMSOL simulation. The varied compression strain corresponds to the injected forces of 25, 50, 75, and 100 nN.

was related to oxygen vacancies, which were possible as defect states responsible for the pinning of the Fermi level [39]. Furthermore, the negative polar surface exhibits lower chemical activity than the Zn-terminated top surface, and the silver electrode acts as inert contact, leading to high barrier height. The interface contact is similar to the one in our study, where the lateral surface of ZnO-NF offers less chemical activity than the c-plane.

In summary, the phenomenon of decreasing forward current magnitudes under the application of excessive compressive forces is well elucidated by the Cheung–Cheung model. Consequently, the imposition of further compressive strain by the AFM tip, composed of aluminum (Al), results in an incremental rise in the Schottky barrier height magnitude, as delineated by (1) and (5). This augmentation of the barrier height results in a widening of the space charge (SC) region, which propagates deeper into the zinc oxide nanowire (ZnO-NF) structure. The expansion of the depleted SC region serves as the underlying mechanism responsible for the observed diminution in current intensity.

A comparable piezoelectric modulation phenomenon accompanied by barrier height increase was observed for the Ag/ZnO and Au/ZnO nanowire junctions [40], where, the application of substantial compressive forces ranging from 100 to 500 nN induced compression strain diminishing the current intensity.

Additionally, an analogous phenomenon of current attenuation under compressive strain was also observed in the FTO/ZnO-NW junction [41].

In order to correlate the simulation and experimental results data, we illustrate in Fig. 11 the variation of barrier height, determined by the Cheung–Cheung model, under different applied compressive strains. The compressive strain was quantified as the relative change in fiber diameter $(\Delta d/d_0)$, where d and d_0 represent the diameters of strained and unstrained ZnO-NF, respectively. The FEM simulation distinctly visualizes the strained ZnO-NF, as depicted by the vertical colored bar (see Fig. 6).

As evident in Fig. 11, a linear increase in barrier height is observed upon the application of compressive strain. The data exhibits an excellent linear fit, with an R-squared value of 0.994, indicating a robust correlation. Significantly, the slope of this linear plot enables the deduction of the piezoelectric coefficient d_{15} [pm/V] based on the following equation

$$\frac{\Delta\phi_B/q}{-\Delta\varepsilon_\perp} = \frac{W_{\text{piezo}}}{\frac{2\varepsilon_{eff}}{e_{15}}}, \tag{11}$$

where ε_{eff} and e_{15} are the effective dielectric constant and the piezoelectric constant of ZnO, respectively. In the case of compression strain, the sign of $\varepsilon_\perp$ is negative, consequently yielding a positive value.

Utilizing this relationship, the effective piezoelectric constant $d_{15} = \frac{2\varepsilon_{eff}}{e_{15}}$ can be estimated by the relation

$$d_{15} = \frac{W_{\text{piezo}}}{\text{slope}}, \tag{12}$$

where W_{piezo} is the piezo width in the depth of the ZnO-NF determined from the FEM simulation, and the slope of Fig. 11 is expressed in volts. The numerical value of slope was found to be 764.87 mV, and W_{piezo} ranged from 0.1–0.8 nm. Consequently, the estimated average value of d_{15} was -8.82 ± 1.50 pm/V, which is in satisfactory agreement with previous reports ($d_{15} = -10.05$ pm/V) [42, 43].

Notably, Fig. 11 establishes a compelling correlation between two distinct results, namely the experimental I–V measurements and the simulated piezotronic behavior of the ZnO-NFs via finite element modeling. Overall, the model demonstrates exceptional performance in characterizing the piezotronic properties of ZnO-NFs.

Building upon the demonstrated coupling between electrical and piezoelectric properties, we propose a piezosensor device based on the junction between AFM tip (Al) and ZnO-NF. This architecture uses the synergistic interplay of these phenomena to enable the high sensitivity of the piezoelectric sensor.

Figure 12 elucidates a linear correlation between the applied mechanical force and the corresponding forward current output response from the piezosensor device. Such a relationship exhibits an inversely proportional nature, wherein the magnitude of the output current undergoes a monotonic reduction as the applied force is incrementally augmented. Notably, upon subjecting the device to a substantial compressive force of 100 nN, the Schottky barrier is effectively modulated to a state that precludes any appreciable current flow, effectively switching off the conductive characteristics of the device.

The results unambiguously demonstrate a direct proportionality between the applied transverse forces and the corresponding output current response from the device. Moreover, this observed behavior is consistent with the findings reported by Xinqin Liao et al. [41] for junction based on FTO/ZnO-NW as depicted above, wherein a similar correlation was established between the current and varying load conditions in in our ZnO-NFs.

In accordance with the formulation proposed by Xinqin Liao et al. [41], the sensitivity S of the piezosensor can be quantitatively defined as

$$S = \frac{(\Delta I/I_0)}{\Delta F}, \tag{13}$$

where I_0 represents the current density under unloading conditions, and F is the applied external force applied by the AFM tip (Al) on the top of the ZnO-NF. In the present study, the differential current density (ΔI) was calculated as the difference between the current responses under loaded and unloaded conditions, evaluated at an applied bias voltage of 10 V.

Referring to Fig. 12, the sensitivity S of the piezotronic device can be quantified as -1.2×10^{-2} N^{-1} or -1.22×10^{-4} gf^{-1}, where 1 gf was equal to 0.0098 N as defined by Xinqin Liao et al. [41].

Alternatively, the sensitivity is defined as the slope of Fig. 12 and can be expressed in terms of the following formula $S = \Delta I/\Delta F$. Employing the aforementioned formulation, the evaluated sensitivity of the piezosensor device in the present study was found to be 147 mA/N. This result demonstrates improved consistency compared to previous reports for the FTO/ZnO-NR junction found by Xinqin Liao et al. [41] (55 mA/N). Furthermore, our obtained value significantly exceeds the sensitivity reported for GaN-NW devices (2.35 mV/nN) [44].

The proposed device architecture, incorporating an aluminum-coated atomic force microscope (AFM) tip as the top electrode, exhibits superior performance characteristics relative to the conventional FTO electrode/ZnO-NR configuration. Moreover, as evidenced in Fig. 12, the fabricated sensors exhibit an excellent linear response to the applied external force over the investigated range and exhibit application prospects in the detection of weak dynamic force.

It is crucial to note that the reported sensitivity value is limited to the response of an individual ZnO-NF, considered a single current source. In contrast, for a matrix or collective assembly of ZnO-NF, multiple current sources would be solicited, potentially leading to a significantly enhanced sensitivity. As a prospective direction for future work, a multi-scale analysis spanning from single nanofiber properties to macroscopic device fabrication and characterization would be highly beneficial. Such an approach would enable the establishment of a quantitative relationship between the intrinsic material

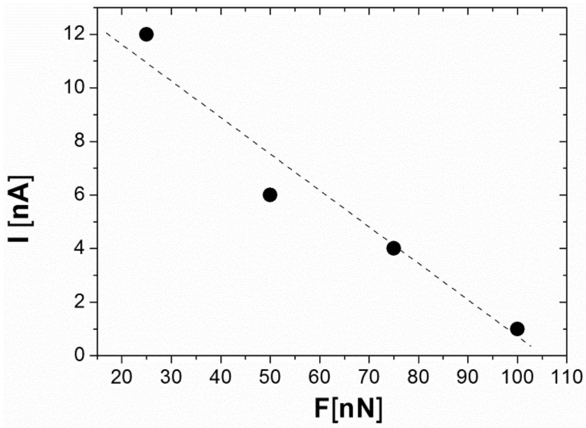

Fig. 12. Linear relationship between applied force and output forward current recorded when ZnO-NW is under mechanical bending at 10 V.

properties of ZnO nanowires and their piezogeneration capabilities, ultimately guiding the design and optimization of efficient piezogenerator devices.

4. Conclusions

In conclusion, we have successfully demonstrated the viability of employing a low-cost aluminum-coated atomic force microscope (AFM) tip as an electrode to obtain rectifying contact, circumventing the need for conventional noble metal coatings. It was observed that this electrode configuration achieved a substantial Schottky barrier height modulation ranging from 250 to 750 meV, which is comparable to noble metal counterparts.

The FEM simulations elucidate that barrier height modulation arises from the coupled piezoelectric and semiconducting properties of ZnO-NFs. In the software, external forces are designated as input parameters, while piezopotential and displacement are the output parameters. Notably, our analysis of the simulation results revealed a maximum piezopotential of -2500 mV under an applied force of 100 nN, in good agreement with the reported works. Furthermore, the simulation study conclusively demonstrated that the modulation of the barrier height was facilitated by piezotronic properties. The application of excessive strain impedes the flow of forward current, with piezoelectricity identified as the primary mechanism responsible for this decrease in forward current. We have observed that excessive bending results in a significant reduction in current intensity, eventually leading to the complete blocking of forward current.

By synergistically combining the simulation output parameters with the experimental I–V characteristics, we derived an average value of the piezoelectric coefficient d_{15} as 8.82 pm/V, which is in excellent agreement with literature reports. We also conclude that such a method as the one developed in this work gives an effective way to characterize some intrinsic properties of ZnO-NFs. This agreement between theoretical calculations and empirical data solidifies confidence in the robustness and accuracy of our simulation approach, which can serve as a reliable platform for further investigations and design optimizations pertaining to ZnO-NF systems and their device applications.

Based on a single ZnO-NF, we realized a piezo-nano-sensor exhibiting a sensitivity value of 147 mA/N at a bias voltage of 10 V. This performance demonstrates improved consistency compared to previously reported piezosensors, such as the FTO/ZnO-NR junction configuration, underscoring the potential of our proposed device architecture.

References

[1] X. Yang, F. Liu, G. Duan, B. Cao, L. Zhang, *CrystEngComm* **19**, 4983 (2017).

[2] A. Tadji, A. Abderrahmane, M. Zerdali, S. Hamzaoui, *Mater. Today Commun.* **31**, 103789 (2022).

[3] L. Xu, Y.L. Hu, C. Pelligra, C.H. Chen, L. Jin, H. Huang, S.L. Suib, *Chem. Mater.* **21**, 2875 (2009).

[4] A. Tab, A. Abderrahmane, Y. Bakha, S. Hamzaoui, M. Zerdali, *Optik* **194**, 1 (2019).

[5] M. Zerdali, F. Bechiri, S. Hamzaoui, F.H. Teherani, D.J. Rogers, V.E. Sandana, P. Bove, P. Djemia, Y. Roussigné, *Proc. SPIE* **10105**, 1010514 (2017).

[6] X. Wang, W. Peng, C. Pan, Z.L. Wang, *Semicond. Sci. Technol.* **32**, 043005 (2017).

[7] Y. Dong, L.J. Brillson, *J. Electron. Mater.* **37**, 743 (2008).

[8] K. Ip, G.T. Thaler, H. Yang, S.Y. Han, Y. Li, D.P. Norton, S.J. Pearton, S. Jang, F. Ren, *J. Cryst. Growth* **287**, 149 (2006).

[9] A.J. Chiquito, C.A. Amorim, O.M. Berengue, L.S. Araujo, E.P. Bernardo, E.R. Leite, *J. Phys. Condens. Matter* **24**, 225303 (2012).

[10] J.W. Lee, J.-H. Kim, S.K. Han, S.-K. Hong, J.Y. Lee, S.I. Hong, T. Yao, *J. Cryst. Growth* **312**, 238 (2010).

[11] V. Consonni, A.M. Lord, *Nano Energy* **83**, 105789 (2021).

[12] Y. Shao, J. Yoon, H. Kim, T. Lee, W. Lu, *Appl. Surf. Sci.* **301**, 2 (2014).

[13] L.J. Brillson, Y. Lu, *J. Appl. Phys.* **109**, 121301 (2011).

[14] R. Ghosh, *Nano Energy* **113**, 108606 (2023).

[15] J.L. Eduardo-River, N. Muñoz-Aguirre, G.J. Gutiérrez-Paredes, P.A. Tamayo-Meza, A.A. Zapata, L. Martínez-Pérez, *Rev. Mex. Fis.* **64**, 655 (2018).

[16] P. Feng, Q. Wan, T.H. Wang, *Appl. Phys. Lett.* **87**, 21 (2005).

[17] A. Schejn, M. Frégnaux, J.-M. Commenge, L. Balan, L. Falk, R. Schneider, *Nanotechnology* **25**, 145606 (2014).

[18] S. Park, S. Park, S. Lee, H.W. Kim, C. Lee, *Sens. Actuators B* **202**, 840 (2014).

[19] C.A. Dimitriadis, J.I. Lee, P. Patsalas, S. Logothetidis, D.H. Tassis, J. Brini, G. Kamarinos, *J. Appl Phys.* **85**, 4238 (1999).

[20] Y. Shao, J. Yoon, H. Kim, T. Lee, W. Lu, *Appl. Surf. Sci.* **301**, 2 (2014).

[21] L.J. Brillson, Y. Lu, *J. Appl. Phys.* **109**, 12 (2011).

[22] M. Zerdali, F. Bechiri I. Rahmoun, M. Adnane, T. Sahraoui, S. Hamzaoui, *Eur. Phys. J. Appl. Phys.* **61**, 30101 (2013).

[23] J. Yang, Z. Li, X. Xin, X. Gao, X. Yuan, Z. Wang, Z. Yu, X. Wang, J. Zhou, S. Dong, *Sci. Adv.* **5**, 1 (2019).

[24] J. Cardoso, F.F. Oliveira, M.P. Proenca, J. Ventura, *Nanomaterials* **8**, 354 (2018).

[25] R. Tao, R. Hinchet, G. Ardila, L. Montès, M. Mouis, in: *2014 10th Conf. on Ph.D. Research in Microelectronics and Electronics (PRIME), Grenoble (France)*, 2014, p. 1.

[26] R. Hinchet, J. Ferreira, J. Keraudy, G. Ardila, E. Pauliac-Vaujour, M. Mouis, L. Montčs in: *2012 Int. Electron Devices Meeting, San Francisco (CA)*, 2012, p. 6.2.1.

[27] L. Zhu, Y. Xiang, Y. Liu, K. Geng, R. Yao, B. Li, *Sens. Actuators A* **341**, 113552 (2022).

[28] R.S. Kammel, R.S. Sabry, *J. Sci. Adv. Mater. Dev.* **4**, 420 (2019).

[29] A. Khan, M. Hussain, O. Nur, M. Willande, *J. Phys. D Appl. Phys.* **47**, 345102, 1 (2014).

[30] Y. Zhang, Y. Liu, Z.L. Wang, *Adv. Mater.* **23**, 3004 (2011).

[31] F. Bernardini, V. Fiorentini, D. Vanderbilt, *Phys. Rev. B* **56**, R10024 (1997).

[32] Q. Yu, R. Ge, J. Wen, T. Du, J. Zhai, S. Liu, L. Wang, Y. Qin, *Nat. Commun.* **13**, 778 (2022).

[33] Z.L. Wang, J. Song, *Science* **312**, 242 (2006).

[34] Y. Liu, Y. Zhang, Q. Yang, S. Niu, Z.L. Wang, *Nano Energy* **14**, 257 (2015).

[35] F. Bechiri, M. Zerdali, I. Rahmoun, S. Hamzaoui, M. Adnane, T. Sahraoui, *Eur. Phys. J. Appl. Phys.* **61**, 30102 (2013).

[36] S.K. Cheung, N.W. Cheung, *Appl. Phys. Lett.* **49**, 85 (1986).

[37] M. Stamataki, D. Tsamakis, J.P. Xanthakis, H.A. Ali, S. Esmaili-Sardari, A.A. Iliadis, *Microelectron. Eng.* **104**, 95 (2013).

[38] P. Keil, T. Fromling, A. Klein, J. Rodel, N. Novak, *J. Appl. Phys.* **121**, 155701 (2017).

[39] M.W. Allen, S.M. Durbin, *Appl. Phys. Lett.* **92**, 122110 (2008).

[40] W. Han, Y. Zhou, Y. Zhang, C.-Y. Chen, L. Lin, X. Wang, S. Wang, Z.L. Wang, *ACS Nano* **6**, 3760 (2012).

[41] X. Liao, X. Yan, P. Lin, S. Lu, Y. Tian, Y. Zhang, *ACS Appl. Mater. Interfaces* **7**, 1602 (2015).

[42] Ü. Özgür, Ya.I. Alivov, C. Liu, A. Teke, M.A. Reshchikov, S. Doğan, V. Avrutin, S.-J. Cho, H. Morkoç, *J. Appl. Phys.* **98**, 041301 (2005).

[43] B.H. Nguyen, X. Zhuang, T. Rabczuk, *Comput. Methods Appl. Mech. Eng.* **346**, 1074 (2018).

[44] X. Xu, A. Potie R. Songmuang, J.W. Lee, B. Bercu, T. Baron, B. Salem, L. Montes, *Nanotechnology* **22**, 105704 (2011).